WILEY-VCH

DOI: 10.1002/ ((please add manuscript number))
Article type: Research Article

High-Throughput Screening of Low-Bandgap Organic Semiconductors for Photovoltaic Applications: In the Search for Correlations

Alfonsina Abat Amelenan Torimtubun,[a] Matías-Jesús Alonso Navarro,[b,c] Arianna Quesada-Ramírez,[a] Xabier Rodríguez-Martínez,[d] José L. Segura,[b] Alejandro R. Goñi[a,e] and Mariano Campoy-Quiles*[a]*

Dr. A. A. A. Torimtubun, A. Quesada-Ramírez, Prof. A. R. Goñi, Prof. M. Campoy-Quiles
[a] Institute of Materials Science of Barcelona (ICMAB-CSIC)
Campus Universitat Autònoma de Barcelona 08193 Bellatera, Spain
E-mail: atorimtubun@icmab.es, aquesada@icmab.es, agoni@icmab.es, mcampoy@icmab.es

Dr. M. J. A. Navarro, Prof. J. L. Segura
[b] Departamento Química Orgánica I, Facultad Ciencias Químicas
Universidad Complutense de Madrid, E-28040, Madrid, Spain
E-mail: segura@ucm.es

Dr. M. J. A. Navarro
[c] Chemical and Environmental Technology Department, ESCET
Universidad Rey Juan Carlos, E-28933, Madrid, Spain
E-mail: matiasjesus.alonso@urjc.es

Dr. X. Rodríguez-Martínez
[d] Institute for Physical Chemistry, Heidelberg University
Im Neuenheimer Feld 253, 69120 Heidelberg, Germany
E-mail: xabier.rodriguez@pci.uni-heidelberg.de

Prof. A. R. Goñi
[e] ICREA, Passeig Lluís Companys 23, 08010 Barcelona, Spain
E-mail: goni@icmab.es

Keywords: high-throughput screening, low-bandgap organic semiconductors, non-fullerene acceptors, organic photovoltaics, energy offset, statistical analysis

ABSTRACT

Low-bandgap non-fullerene acceptors (NFAs) offer a unique potential for photovoltaic (PV) applications, such as transparent PV and agrovoltaics. Evaluating each new PV system to achieve the optimum thickness, microstructure, and device performance is, however, a complex multiparametric challenge with large time and resource requirements. In this work, we evaluate the photovoltaic potential of low-bandgap donor and NFA materials by combining high-throughput screening and statistical methods. The use of thickness gradients (20–600 nm) facilitated the fabrication of more than 2000 doctor-bladed devices from 24 different low-bandgap blend combinations. The corresponding power conversion efficiencies varied significantly, from 0.06% to 10.45% across materials and thicknesses. The self-consistency of the large dataset allowed to perform a parameter sensitivity study as well as parameter correlation analysis. These revealed that the choice of materials and energy alignment-related features (*i.e.* electron affinity offset, ionization energy offset, band gap, and energy loss) had the largest influence on final device performance, while processing conditions appeared less important for the final efficiencies. Our study demonstrates that high-throughput experimentation is a perfect match for correlation analyses in order to gain a statistically meaningful understanding of these systems, potentially accelerating the discovery of new materials.

INTRODUCTION

Organic photovoltaics (OPVs) are attracting increasing attention owing to their unique traits such as processability in solution, lightweight, large area, flexibility, low-cost fabrication, and tunable properties by molecular design.[1–4] Continuous efforts in materials synthesis, morphology control, and device engineering have pushed the power conversion efficiencies (PCEs) over 19% for single-junction devices and exceeding 20% for tandem configuration.[5–8]

A key development has been the continuous progress of non-fullerene acceptors (NFAs). Specifically, low-bandgap materials with a typical optical bandgap (E_g) lower than 1.6 eV could enhance solar light utilization: The light distribution of the AM 1.5G solar spectrum is such that approximately 51% of solar photon flux is found in the NIR region.[9] Moreover, other appealing physical properties have been found in these materials, including a strong dipole moment and a low exciton binding energy.[10] These low-bandgap NFAs that absorb in the near-infrared (NIR) region have attracted interest in a number of emerging photovoltaic technologies. They have been widely used in semitransparent OPVs for various applications, including agrivoltaics, power-generating windows, heat-insulation, wearable electronics, and building-integrated photovoltaics.[9,11,12] Furthermore, their ability to extend the absorption range to the NIR spectrum has been employed in tandem OPVs,[13–16] ternary OPVs[17–19] and NIR-absorbing organic photodetectors.[20–22]

Despite such great progress, several drawbacks impair the practical applications of low-bandgap OPVs, which are still far from being a reality. For instance, the inherent narrow bandgaps of these materials often result in a low open-circuit voltage (V_{OC}). Increasing V_{OC} while maintaining high transmittance in visible light and harvesting more photons in the NIR region represents, indeed, a big challenge in semitransparent OPVs.[12] In tandem OPVs, balancing the trade-off between V_{OC} and short-circuit current density (J_{SC}) in the front and rear sub-cells is crucial.[23] Another aspect to consider is the selection of appropriate third components for ternary OPVs.[19] Furthermore, the number of organic materials with bandgap <1 eV and high mobility is very limited. High external quantum efficiencies in the NIR as well as simultaneously very low dark current densities, would be required to achieve high NIR photoresponsivity for NIR-organic photodetectors.[21]

Finding the optimal parameters for active layers in OPVs is a complex, laborious, and time-consuming process. It involves considering a large set of parameters, including intrinsic material properties, extrinsic processing conditions, and device features.[24] This extensive

parameter list should be optimized for each material system. Importantly, there is an infinite number of potential candidates due to the facile chemical tuneability of NFAs, and therefore there is a need to evaluate an unaffordable number of D/A potential combinations. This is particularly true for devices processed using spin-coating following the classical one-variable-at-a-time (Edisonian) optimization approach, in which each of the involved parameters is varied individually. Alternatively, it can be argued that the evaluation of materials would be more relevant if performed in the framework of more scalable deposition methods, and more efficient if carried out using high-throughput screening. Blade-coating has been deemed a promising high-throughput printing technology for lab-to-fab transition in large-area OPV processes.[25–27] A recent study by Zheng *et al.* demonstrated that the hydrodynamic behavior of spin-coating and blade-coating is different, resulting in their distinct blend morphologies and device performances.[28,29] These works [26,30–32] suggested that the whole processing approach must be revisited when transitioning from spin-coating to blade-coating or slot-die coating, compromising the high-throughput experimentation workflow.

Recent studies employed high-throughput methodologies for evaluating the device performance and processing conditions of wide-to-medium bandgap active materials demonstrating much faster evaluation times and accelerated material discovery.[33–36] Importantly, large, self-consistent experimental datasets often result from high-throughput experimentation. Robust statistical methods can be employed in said datasets to uncover hidden patterns and disentangle the correlations between two or more specific parameters.[37] Notably, the self-consistency of the datasets is highly desirable to ensure the reliability of analyses and to minimize the risk of misinterpreting the results, thus solid conclusions can be drawn. Despite its potential benefits, high-throughput studies of low-to-ultralow-bandgap materials remain scarce. The combination of fast experimental approaches and correlation analyses could then accelerate the development of PV applications based on these highly promising and versatile materials.

In this contribution, we present a systematic and efficient exploration of 24 blade coated low-bandgap systems using high-throughput experimentation and statistical methods to identify their photovoltaic potential and the underlying features of importance. More precisely, we have fabricated over 2,000 solar cells based on 5 low-bandgap donors, 8 low-bandgap acceptors, and a fullerene reference. The extensive experimental data collected from all samples was employed to conduct a parameter sensitivity statistical study, unveiling that the choice of materials and electronic features related to energy level alignment (*i.e.* electron affinity offset, ionization energy offset, band gap, and energy loss) play the most significant role in the device performance of low-bandgap OPVs. Recently, a discussion concerning the impact of energy level offset on photovoltaic performance has become a hot and controversial topic in the OPV field.[38–40] We then propose the use of correlation analysis to gain a deeper understanding of the relationship between electronic features and the overall device performance for the most promising material systems (*i.e.* PTB7-Th based blends), as those were found to be the most important parameters affecting our studied devices.

RESULTS AND DISCUSSION

Physical properties of semiconducting materials

To reveal the most influential parameters on the device performance and potential photovoltaic applications of low-bandgap OPVs, we studied a large combinatorial set of representative donor-acceptor pairs: the widely used low-bandgap donor polymers PTB7-Th (PCE10), two examples of the low-bandgap diketopyrrolopyrrole (DPP) polymer family, namely PDPP4T and DPP-DTT, and the novel low-bandgap donors NIP3T and NIP3T-BDT. The latter were synthesized in Prof. Segura's group, and the corresponding synthesis process and material characterization are explained in detail in the Supporting Information. Eight small molecule low-bandgap NFAs were selected as acceptors, including Y6, one of the current state-of-the-

art NFAs, and COTIC-4F, one of the lowest-bandgap NFAs commercially available. The fullerene derivative $PC_{70}BM$ was employed as a wide-bandgap reference. The corresponding chemical structures are shown in Figure 1a. The term "low-bandgap" is employed in this work to refer to materials or blends that have E_g ranging between 0.9 to 1.6 eV, corresponding to the spectroscopic energy range of infrared-A in the NIR range.[41] The E_g of the studied materials was determined by the Tauc plot method from the UV-vis absorption band, as displayed in Figure S1 and Table S1.

The energy levels of the donor and acceptor materials are shown in Figure 1b, based on previously reported values determined primarily by thin film photoelectron spectroscopy or cyclic voltammetry.[42–45] When comparing donor materials, the introduction of strong acceptor moiety of DPP yields a highest occupied molecular orbital (HOMO) and lowest unoccupied molecular orbital (LUMO) energy levels which are shifted ca. 0.5 eV and 0.17 eV, respectively, compared to those of PTB7-Th. In the case of the NIP3Ts polymer family, the introduction of a strong electron-withdrawing imide group connected through an electron-accepting pyrazine moiety stabilized their LUMO levels, whereas the introduction of electron-donating oligothiophenes or alkoxy-thiophene derivatives brings closer their HOMO levels compared to those of DPP-based polymers. Notably, the D-A character of the NIP3T core in NIP3T-based polymers possesses segregated HOMO and LUMO states[46], unlike PTB7-Th and DPPs, which have both states in the same region.[47] In summary, the bandgaps of the donors decrease from PTB7-Th, to the DPP, and to the two NIP3T polymers.

On the other hand, when comparing acceptor materials with similar conjugated backbone, alkyl chain modification in conjugated core and chlorination in electron-withdrawing groups (Y6 *vs.* BTP-eC9) has a moderate influence on the electronic structure. The same is observed for the silicon to carbon substitution at the central donor D'-D-D' core (SiOTIC-4F *vs.* COTIC-4F). The former modification shifts the LUMO level up to 0.11 eV, while the latter shifts only by 0.05 eV. Increasing the LUMO levels of the acceptor with respect to the HOMO

levels of the donor is expected to promote an enhancement in V_{OC}, provided that the materials show similar levels of recombination. For instance, with respect to the HOMO level of PTB7-Th donor, the increase of O-IDTBR and $PC_{70}BM$ LUMO levels to −3.60 eV and −3.85 eV would result in higher V_{OC} values than for the other NFAs due to the higher offset between the LUMO of acceptor and the HOMO of PTB7-Th donor (ΔE_{DA}).

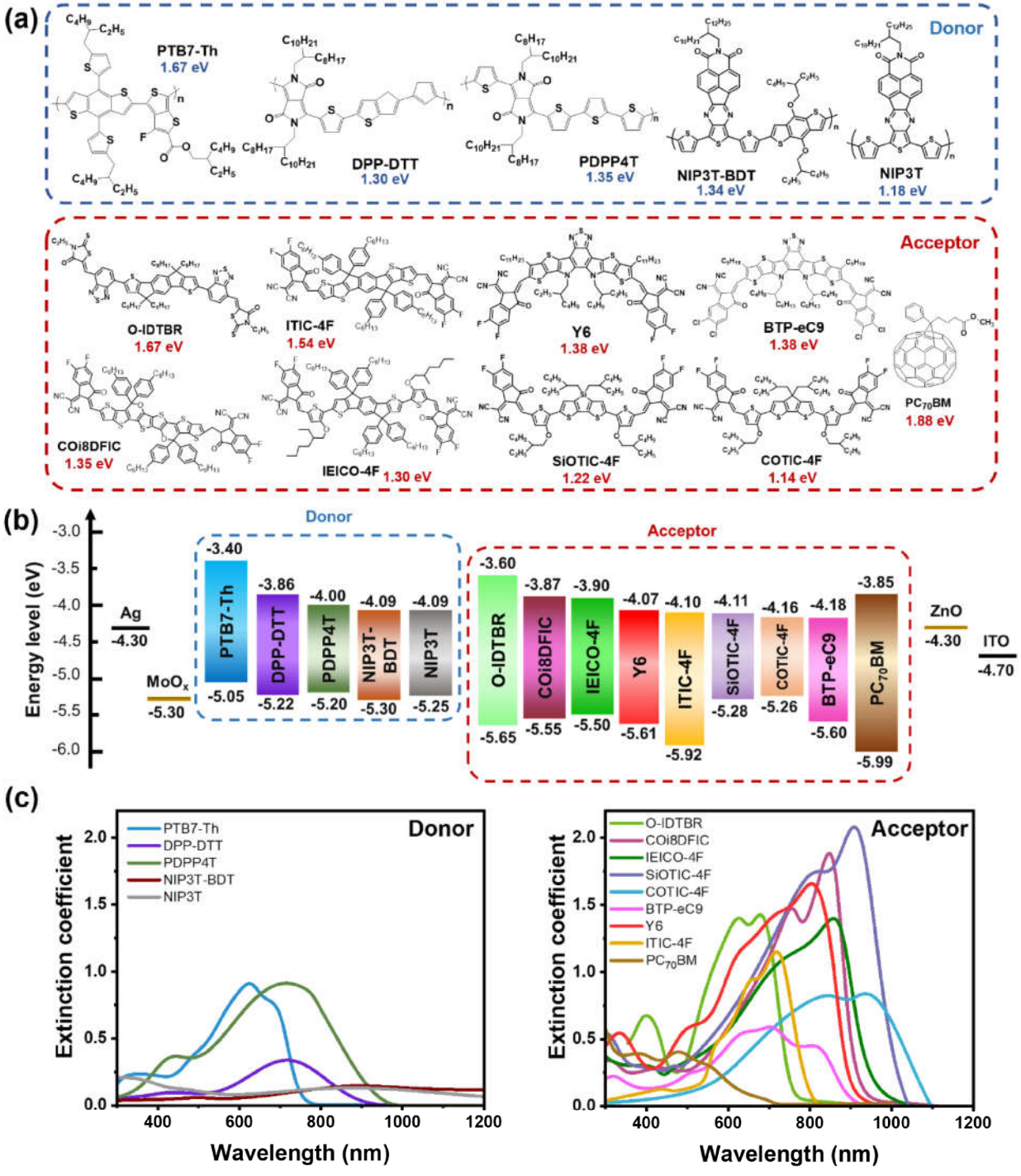

Figure 1. Material properties of the studied low-bandgap donor and acceptor semiconductors: (a) chemical structure, (b) energetic levels in inverted device structure, and (c) extinction coefficient of donors (left graph) and acceptors (right graph) measured by variable angle spectroscopic ellipsometry.

It has been argued that the energy difference in LUMO levels between donor and NFAs, defined as electron affinity (EA) offset, should be around 0.3 eV for efficient charge transfer.[48] Except for O-IDTBR, the EA offset between the PTB7-Th donor and NFAs is around 0.5 to 0.7 eV, which leads to sufficiently efficient electron transfer from the donor to the acceptor. At the most elementary view, the energetic offset between HOMO levels of donor and acceptor components, defined as ionization energy (IE) offset, could indirectly be related to the energy loss ($E_{loss} = E_g - eV_{OC}$) in bulk heterojunction blends.[10,38,49] For instance, and as reported, the up-shifted HOMO levels observed in SiOTIC-4F and COTIC-4F are relatively higher than the other NFAs (with HOMO levels in the range of −5.5 to −5.9 eV), which is desirable for mitigating losses, thus reducing E_{loss}.[43]

Figure 1c shows the extinction coefficient (κ) values of donor and acceptor materials in thin film, obtained by variable angle spectroscopy ellipsometry (VASE) measurements. The associated refractive indices (n) are presented in Figure S2. The corresponding optical data are summarized in Table S1. In general, the energy levels and basic optical behavior will be given by the properties of the conjugated backbone.[50] Compared to PTB7-Th, the absorption redshift observed in PDPP4T and DPP-DTT leads to a partial overlapping with the absorption of the NFAs. NIP3T and NIP3T-BDT exhibit a further redshifted absorption with, however, a low oscillator strength. Following Fermi´s golden rule, the low κ values in these two polymers may originate from their segregated molecular orbital topology[51] in comparison with the other polymers. This precise chemical moiety combination altered the HOMO/LUMO wavefunction superposition, leading to lower oscillation strength and, thus intensity of the UV-Vis profile.[46] On the other hand, the set of NFAs can harvest light across a broad spectrum, spanning from 500 nm to 1100 nm, with the specific range varying depending on the molecule. Conversely, $PC_{70}BM$ is known to contribute little to the overall absorption of the blend. Moreover, the

conjugated length in NFAs could influence the κ values. For instance, COi8DFIC, which has the longest fused conjugated rings, shows higher κ values and a more red-shifted absorption onset compared to Y6 to O-IDTBR. This can be attributed to the increased delocalization of π electrons as the conjugated length increases. However, this is not always the case. It is observed that BTP-eC9 and ITIC-4F, which have the same conjugated length as Y6, exhibit a blue-shifted absorption onset and lower κ values, which may originate from the differences in molecular conformation and planarity.[50] Interestingly, this set of NFAs shows a variable degree of complementary absorption with respect to the studied donors, which enables a variable degree of transparency in the visible, in some cases, extending the light absorption from 400 nm to 1100 nm, as shown in Figure S3 and Figure S4. Thus, we may expect an increased short-circuit current density (J_{SC}) of the solar cells based on complementary absorption with respect to those with overlapping absorption as well as compared to those based on the $PC_{70}BM$ fullerene counterpart.

High-throughput experimental screening

Herein, a high-throughput strategy based on lateral parametric gradients substitutes the traditional sample-by-sample Edisonian methodology in the screening of low-bandgap OPV best material system. Figure 2a illustrates the fabricated 24 device arrays arranged on a large aspect-ratio, pre-patterned ITO substrate with equivalent left- and right-side devices. Thus, 12 different values of the targeted parameter are available on each substrate, with one replica per value. An active layer thickness gradient is illustrated over the long axis of the substrate. The processing of gradient thickness was accomplished by blade coating using a modified control electronic unit that allows for adjusting the velocity and acceleration of the blade during deposition, as reported elsewhere.[33,34,36] The speed of the blade is generally the main factor affecting film thickness, given a certain amount of solution and viscosity. In other words, a faster speed, a larger quantity, and greater viscosity result in a thicker film if the conditions for

the viscous drag regime (also called the Landau-Levich regime) are fulfilled.[47,48] Due to the length of our substrate (a typical microscope slide length of 7.5 cm) and to minimize the thickness differences from batch to batch, we use the same solution volume of 60 μL for each deposition. The thickness gradients were fabricated by linearly decelerating the blade during deposition from 90 to 10 mm s^{-1}. A decreasing speed ramp coupled with a sufficient amount of solution enables the formation of steeper thickness gradients from the thick to the thin side. Typically, we have obtained thickness gradients spanning from 500 nm to 20 nm. As a result of this fabrication methodology, a large device dataset from over 2,000 cells featuring 24 different low-bandgap blend systems with various processing conditions was effectively evaluated in this study.

Conducting an extensive characterization and data processing of thousands of OPV cells could be inevitably overwhelming since it requires a long characterization time and a high risk of human error. A measuring-intensive approach using a custom-built automated multiplexer platform was designed to decrease characterization time and reduce reproducibility errors significantly, as reported elsewhere.[54] Exemplarily, Figure 2b shows a total of 24 generated *J-V* curves in which 12 unique PTB7-Th:COTIC-4F active layer thickness values (two replicas one at each side) were measured automatically by the multiplexer in a single run. Then, we generate a photovoltaic figures-of-merit database containing PCE, V_{OC}, J_{SC}, and fill factor (FF) values as a function of active layer thickness (see Figure 2c). The use of thickness gradients allows us to concurrently identify the optimum active layer thickness and thickness sensitivity on each blend system. Given the PTB7-Th:COTIC-4F blend as an example, their PCE decreases slightly as the active layer thickness increases, showing a PCE maximum at around 110 nm. As devices become thicker, a progressive decay of PCE is mostly driven by an FF reduction while J_{SC} and V_{OC} values remain constant. The reason behind PTB7-Th:COTIC-4F photovoltaic figures-of-merit thickness dependence will be elucidated in more detail along with 23 other different D:A low-bandgap blends in the following sections. In addition, our group established

a motorized external quantum efficiency (EQE) measurement system, which, together with an automated multiplexer for *J-V* characterization, enables the quick and reliable measurement of wavelength-sensitive information for all cells within one substrate in an automated manner.[54] Figure 2d shows the EQE spectra of the PTB7-Th:COTIC-4F cells as a function of active layer thickness. Consistent with the J_{SC} trend observed in Figure 2c, the corresponding EQE values increase until the optimal thickness is reached, slightly decreasing as cells become thicker. Interestingly, a change in EQE spectra is observed for thicker active layers, exhibiting higher EQE in the donor region than the acceptor region. This is likely due to the fact that the donor extinction coefficients are lower than that of the used acceptors (see Fig. 1c), such that thicker films can effectively absorb more light in the donor spectral region.

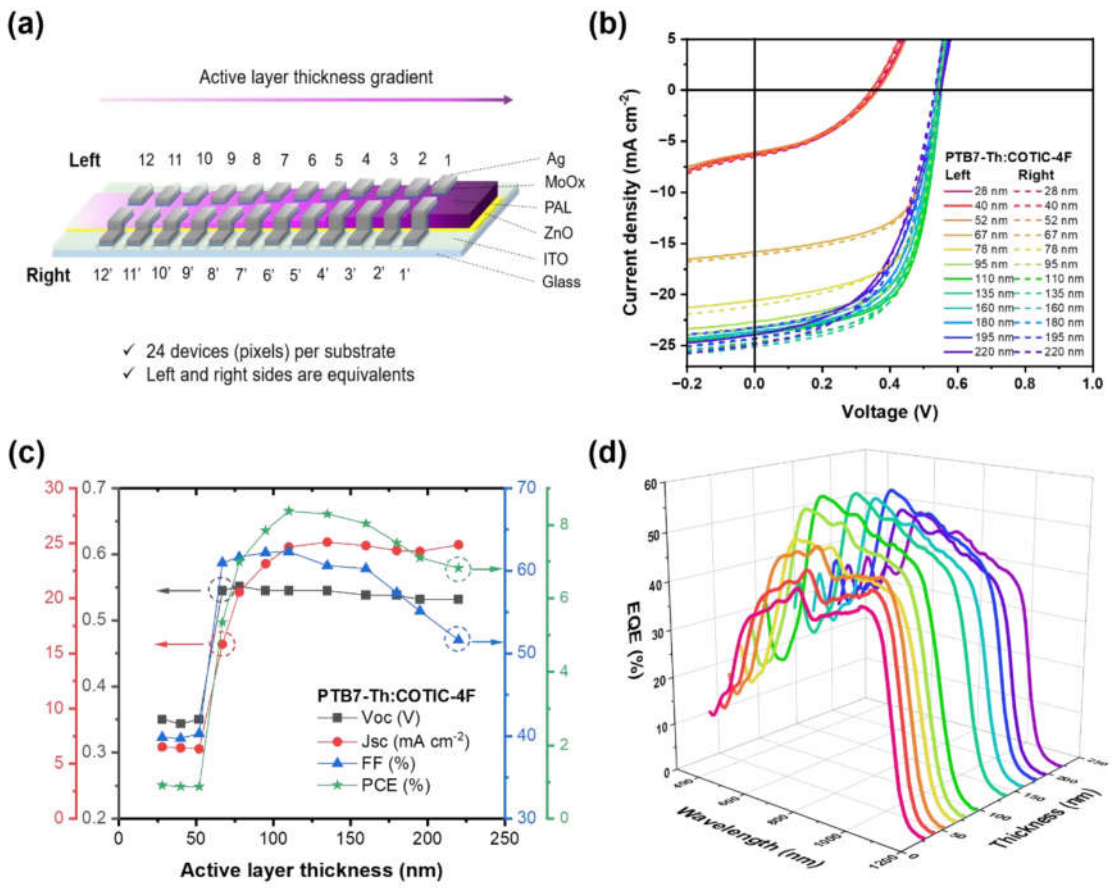

Figure 2. (a) Schematic illustration of an array of 24 devices arranged on a large aspect-ratio, pre-patterned ITO substrate. (b) *J-V* characteristics under 1 sun illumination, (c) extracted device

performance parameters, and (d) external quantum efficiency (EQE) spectra of blade-coated PTB7-Th:COTIC-4F based OPVs with thickness gradient under high-throughput experimentation workflow.

Following the high-throughput lateral gradient workflow, the optimum active layer thickness of each low-bandgap D:A combination is straightforwardly identified. The *JV* characteristics of the blade-coated champion devices obtained keeping the same donor (PTB7-Th) but varying the acceptor, are presented in Figure 3a, whereas those of other D:A blends are depicted in Figure S5a–b. The corresponding photovoltaic parameters for the best cells of all 24 combinations are summarized in Table 1. For the sake of discussion, these devices are divided into three groups based on their photovoltaic performance. The devices prepared by blending with PTB7-Th will be referred to as group 1. They possess appropriate energy-level offsets between PTB7-Th and the acceptors (EA offset ranging from 0.20 to 0.78 eV, IE offset of 0.21 to 0.94 eV), and exhibited high J_{SC} (14.3 – 24.6 mA.cm^{-2}), V_{OC} (0.5 – 1.0 V), FF (60 – 68 %), and PCE (7.4 – 10.4%). These results indicate that the charge generation in these devices was efficient and the V_{OC} differences mainly stemmed from the different ΔE_{DA} offsets, while J_{SC} differences originated from the different absorption coefficients. It is worth mentioning that the blade-coated devices based on PTB7-Th:COTIC-4F yielded a PCE of 8.38%, with a V_{OC} of 0.54 V, a J_{SC} of 24.66 mA.cm^{-2}, and an FF of 62.31%, demonstrating, to the best of our knowledge, the highest PCE value for an inverted configuration among the reported studies of (mostly spin-coated) PTB7-Th:COTIC-4F based OPVs.[43,55–57] This PCE improvement, although using a more scalable deposition technique like blade-coating, demonstrates the potential of applying lateral gradients towards accelerating the up-scaling of high-performance, low-bandgap OPV materials.

The devices using PDPP4T and DPP-DTT as donors constituted group 2. Compared to the first group, the energy-level offsets of the blend materials in this group were lower. EA offsets ranged from negative values to 0.30 eV, while IE offsets varied from almost 0 to 0.72

eV. Although the corresponding devices exhibited considerable FF (53 – 67%), their V_{OC} (0.4 – 0.6 V) and, more importantly, J_{SC} (4.4 – 10.2 mA cm^{-2}) values are lower than those of group 1, indicating relatively severe non-radiative charge recombination in these DPPs-based devices. In fact, J_{SC}s of DPPs blends are observed to be between two and six times lower than those for PTB7-Th blends. As the DPP donors have a narrower bandgap than PTB7-Th, these J_{SC} differences may originate from a more panchromatic absorption between low-bandgap NFAs and PTB7-Th donor than those of DPP counterparts.

Group 3 included the devices based on the newly synthesized NIP3T-BDT and NIP3T donors. The IE offsets of these devices were relatively large (almost 0 to 0.74 eV), while mostly negative EA offsets were observed. Compared to groups 1 and 2, the FF values of group 3 are the lowest (35 – 45 %) with also very low V_{OC} (0.35 – 0.58 V) and J_{SC} (almost 0 to 9.7 mA cm^{-2}). These results suggest that morphological issues and charge recombination in these devices severely affect charge separation and collection. Consistently, it was discovered that group 1 has the lowest E_{loss} values, ranging from 0.57 eV to 0.88 eV, as compared to those of the devices in group 2 (0.62 – 0.94 eV) and group 3 (0.65 – 1.43 eV). Figure 3b presents the EQE spectra of devices of the PTB7-Th based system, whereas Figure S5c–d shows the EQEs for the devices in groups 2 and 3. As shown in Figure 3b, devices in group 1 exhibit strong photo-responses, with the maximum EQE values exceeding 50%, and a broad response ranging from 300 to 1150 nm. In contrast, devices in group 2 possess narrower response ranges and their maximum EQE values did not achieve even 25%. Although the devices in group 3 displayed a broad response range from 300 to 1150 nm, their EQE values were less than 20%.

In general, the maximum PCEs of spin-coated OPV devices are achieved with thicknesses of ca. 100 nm. However, here we show that the use of blade-coating results in optimum active-layer thicknesses over 100 nm for most blends (see Table 1). This is in good agreement with the results of Zhang *et al*.[25], demonstrating that blade-coating could balance the charge-carrier mobilities and improve film morphologies, thus affecting the relationship of

device performance with active layer thickness. Notably, most blends in DPPs-based systems have optimum active layer thickness exceeding 200 nm, which meets a thickness requirement for thick-film devices to avoid device shunts in large-area processing.[25,58] For completeness, we show in Figure 3c–f, Figure S6, and Figure S7 the detailed photovoltaic figures-of-merits of the blends based on PTB7-Ths, DPPs, and NIP3Ts as a function of active layer thickness ranging from 20 nm to 600 nm, respectively. As depicted in Figures 3c, S6a, and S7a, for PTB7-Th blended with COi8DFIC, ITIC-4F, COTIC-4F, SiOTIC-4F, BTP-eC9, or $PC_{70}BM$ and all NIP3Ts based devices, the PCE decreases with increasing active-layer thickness above ca. 200 nm, showing a single PCE maximum typically ca. 100 nm. This is attributed to the gradual decrease of their J_{SC} and FF values as the film thickness increases above 200 nm. Since the charge carriers need to travel longer distances to reach the respective electrodes in thick films, the reduction of J_{SC} and FF values could be due to the low charge mobility of the PTB7-Th and NIP3Ts donors, which increases the likelihood of non-radiative recombination.[58]

On the other hand, PTB7-Th blended with Y6, IEICO-4F, or O-IDTBR and all DPP based devices show constant J_{SC} and FF values at thicker active layer, thus exhibiting a more thickness-insensitive PCE. In the case of DPPs-based devices, such behavior originates from the high mobility of the DPPs donors. Regardless of the blends, the V_{OC} remains nearly unchanged as the film thickness increases from ~80 nm to 600 nm. Nevertheless, when active layer thickness falls below 50 nm, a pronounced drop in V_{OC} is observed. This reduction is concomitant with the increase in series resistance (see Figure S8) in very thin films, possibly due to a poorer quality of films and interfaces, particularly between the active layer and buffer layers or electrodes, where defects or impurities can lead to high contact resistances. A detailed study on what makes OPV devices thickness-insensitive will be reported elsewhere[53], highlighting knowledge of materials and devices towards thickness-resilient OPVs.

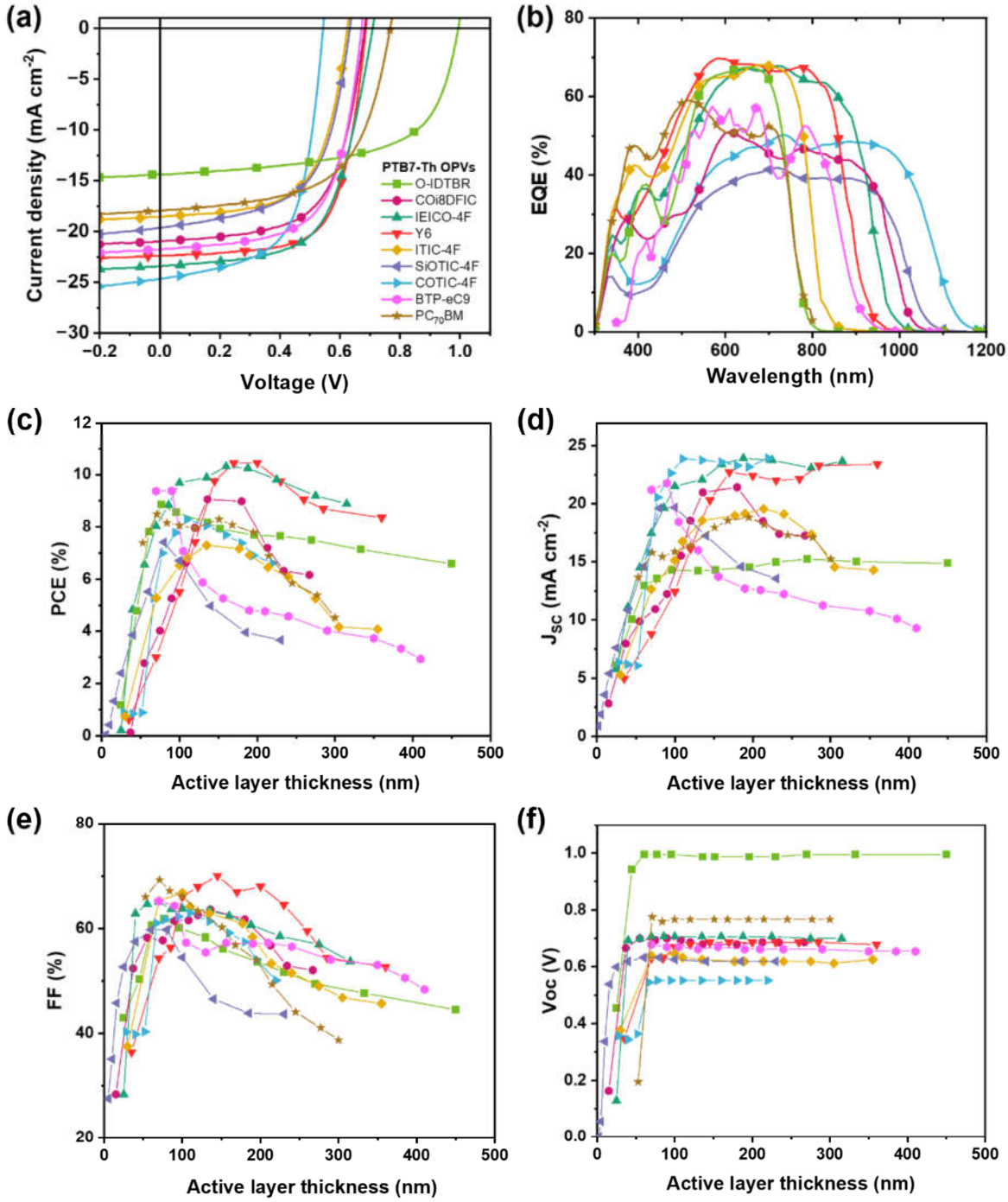

Figure 3. (a) *J-V* characteristics and (b) EQE spectra of PTB7-Th based systems mixed with nine different acceptors materials. Photovoltaic performance parameters of the doctor-bladed PTB7-Th based solar cells, namely (c) PCE, (d) J_{SC}, (e) FF, and (f) V_{OC}, plotted as a function of active layer thickness.

Table 1 *Photovoltaic parameters of the doctor bladed champion solar cells based on PTB7-Th, DPPs, and NIP3Ts systems mixed with different acceptor materials.* [a] $\mathbf{E_g}$ *is the optical energy bandgap determined from Tauc's method from the absorption spectra of the blends.* [b] $\mathbf{E_{loss}}$ *is the energy loss calculated as* $E_{loss} = E_g - qV_{OC}$. $\Delta\boldsymbol{EA}$ *is the electron affinity offset (*$LUMO_D - LUMO_A$*),* $\Delta\boldsymbol{IE}$ *is the ionization potential offset (*$HOMO_D - HOMO_A$*), and* $\boldsymbol{AL_{opt}}$ *is the optimum active layer thickness.*

Donor	Acceptor	E_g [a] (eV)	V_{OC} (V)	J_{SC} (mA cm^{-2})	FF (%)	PCE (%)	ΔEA (eV)	ΔIE (eV)	E_{loss} [b] (eV)	AL_{opt} (nm)
PTB7-Th	Y6	1.40	0.69	22.41	68.00	10.45	0.67	0.56	0.71	200
PTB7-Th	IEICO-4F	1.28	0.71	23.43	62.37	10.32	0.50	0.45	0.57	160
PTB7-Th	BTP-eC9	1.40	0.67	21.78	64.29	9.38	0.78	0.51	0.73	100
PTB7-Th	COi8DFIC	1.30	0.68	20.98	63.57	9.06	0.47	0.55	0.62	135
PTB7-Th	O-IDTBR	1.66	1.00	14.37	61.81	8.84	0.20	0.62	0.66	77
PTB7-Th	$PC_{70}BM$	1.64	0.77	15.81	69.27	8.48	0.45	0.94	0.87	150
PTB7-Th	COTIC-4F	1.15	0.54	24.66	62.31	8.38	0.76	0.21	0.61	110
PTB7-Th	ITIC-4F	1.53	0.65	18.76	67.05	8.12	0.70	0.87	0.88	135
PTB7-Th	SiOTIC-4F	1.22	0.63	19.63	59.76	7.42	0.71	0.23	0.59	80
PDPP4T	IEICO-4F	1.34	0.61	8.01	67.23	3.29	-0.10	0.30	0.73	250
PDPP4T	ITIC-4F	1.37	0.54	8.97	65.63	3.19	0.10	0.72	0.83	160
PDPP4T	Y6	1.37	0.44	10.19	64.0	2.90	0.07	0.41	0.93	145
PDPP4T	BTP-eC9	1.40	0.57	7.48	57.44	2.43	0.18	0.36	0.87	130
PDPP4T	COTIC-4F	1.18	0.46	6.91	64.16	2.04	0.16	0.06	0.72	300
PDPP4T	COi8DFIC	1.35	0.59	4.38	57.04	1.48	-0.13	0.40	0.76	250
DPP-DTT	Y6	1.37	0.49	7.93	60.87	2.38	0.21	0.39	0.88	390
DPP-DTT	IEICO-4F	1.29	0.60	5.08	59.53	1.81	0.04	0.28	0.69	360
DPP-DTT	COTIC-4F	1.13	0.51	5.60	57.83	1.66	0.30	0.04	0.62	110
DPP-DTT	ITIC-4F	1.55	0.61	4.64	52.83	1.48	0.24	0.70	0.94	200
NIP3T-BDT	COTIC-4F	1.11	0.45	9.70	39.25	1.72	0.04	0.01	0.66	85
NIP3T-BDT	$PC_{70}BM$	1.97	0.58	4.68	45.31	1.23	-0.27	0.74	1.39	150
NIP3T-BDT	ITIC-4F	1.15	0.50	5.96	37.06	1.10	-0.02	0.67	0.65	140
NIP3T	$PC_{70}BM$	1.90	0.47	0.41	35.51	0.07	-0.34	0.88	1.43	75
NIP3T	ITIC-4F	1.49	0.35	0.45	29.02	0.06	-0.09	0.81	1.14	85

Meta-analysis in low-bandgap OPVs

A one-way ANOVA analysis was conducted in order to determine the parameters affecting more critically the photovoltaic performance of blade-coated low-bandgap OPV devices. This analysis generates a parameter called the F factor, which measures the variance ratio between the independent variables (electronic features, optical features, processing conditions) and the variation in the dependent output variables (PCE, J_{SC}, FF, or V_{OC}). Essentially, the F factor

serves as a statistical gauge of the significance of a given parameter in determining the final device performance. The ANOVA F-values for the studied parameters are summarized in Table 2, revealing that within the large parameter space explored in all blends, the donor material is the most sensitive performance parameter for low-bandgap OPVs (F = 129). While PTB7-Th devices achieve efficiencies over 10.4%, NIP3T-based devices only yield 0.06%. Then, the second most sensitive parameters (F = 86) are those related to the HOMO/LUMO energy level alignment, such as charge-transfer offsets and energy losses. The least sensitive parameters are the device processing conditions with $F \leq 15$ (solvent, solvent additive, casting temperature, annealing temperature, and blade speed).

Given the importance of the donor material for low-bandgap OPV performance, we then performed a specific ANOVA analysis of devices having the PTB7-Th donor blended with nine different acceptor materials (Table 2). We have found that, in terms of PCE, the choice of acceptor material and electronic features like energy offsets and energy losses have a higher impact than the processing conditions, as for the analysis that included all blends. The impact of electronic features is also high on J_{SC}, confirming that the photo-generated current is very sensitive to the variation of intrinsic material properties, as shown in the previous section. A note of caution should be given here, as the ANOVA analysis only considers existing restricted datasets, since we have not fabricated cells with wider solvent choices or D:A compositions, for example. Moreover, with the limited number of data points, establishing the normal distribution requirement is inaccurate. Nevertheless, our study indicates that, as a rule of thumb, the most critical low-bandgap OPV parameters are, first, the choice of materials, then the energy alignment, and finally the processing features.

Table 2. ANOVA analysis of the parameters varied for all 24 systems (left), and for exclusively those based on PTB7-Th as donor (right).

Property	F-value for all systems	F-value for PTB7-Th OPVs

	PCE	V_{OC}	J_{SC}	FF	PCE	V_{OC}	J_{SC}	FF
Donor materials	158	88	145	99	–	–	–	–
Acceptor materials	29	13	50	12	84	18	145	17
ΔIE (IE_D – IE_A)	82	18	132	14	84	18	145	17
ΔEA (EA_D – EA_A)	86	18	137	15	84	18	145	17
$E_{D\text{-}A}$ (IE_D – EA_A)	56	13	92	13	50	18	70	7
E_{loss}	84	16	141	15	84	18	145	16
Solvent	3	5	4	10	47	18	56	16
Solvent additive	11	4	31	3	35	13	72	3
Casting temperature	11	5	10	14	44	12	51	21
Annealing temperature	15	4	24	4	14	2	22	4
Blade speed	6	5	7	3	8	6	7	3

Once the donor material was determined, PTB7-Th in this case, we performed an ANOVA analysis using a database of more than a thousand devices, the results of which are classified and summarized in Figure 4. To ensure clarity, we fixed threshold values for the dependent variables of the solar cells, namely a V_{OC} greater than 0.3 V, FF greater than 30%, and PCE greater than 0.5%. The numbers in brackets in Figure 4 represent those devices that successfully surpassed the threshold. For instance, an equal number of BTP-eC9 and $PC_{70}BM$-based devices were fabricated; however, one $PC_{70}BM$-based device must be excluded due to its PCE being below 0.5%. The box and whisker plots, which provide a concise overview of the optimization process, also include in the ANOVA analysis variations in the active layer thickness, annealing temperature, casting temperature, solvent, and solvent additives. This, in turn, increases the apparent scatter of the data.

Overall, when considering the different acceptors, the V_{OC} has a lower deviation from the mean values (<0.1), as compared to J_{SC} and FF. For a given donor:acceptor blend, this is typically a consequence of small changes in recombination and the degree of crystallinity of the active layer.[59] Interestingly, the large dispersion in V_{OC} observed for O-IDTBR is likely

due to a variation of the D:A ratio, since for the rest of the blends this ratio was maintained to a similar value of 1:1.5. Varying the D:A ratio may induce microstructural changes in the blend films that affect their energy levels, recombination characteristics as well as the hole mobility and hole transport disorder coefficient.[60] Unlike the V_{OC}, larger dispersions are observed in the values of J_{SC} and FF. The systems with the largest J_{SC} scatter are COi8DFIC (56 devices) and SiOTIC-4F (293 devices). On the other hand, COTIC-4F and IEICO-4F show the highest J_{SC} values, which can be correlated with their high and broad-range EQE responses (see Figure 3b). Notably, a high fluctuation of the average values of J_{SC} across all acceptor materials strongly correlates with the highest ANOVA F values referred to photovoltaic performance. For the FF, even though the scatter is high for each acceptor system, the overall median values are similar. The Y6 system exhibits the highest FF (68%); higher than any value reported in the literature for spin-coated cells.[61] Finally, the PCE reveals that the most promising acceptor blended with PTB7-Th is Y6 due to its concurrently high J_{SC} and FF values.

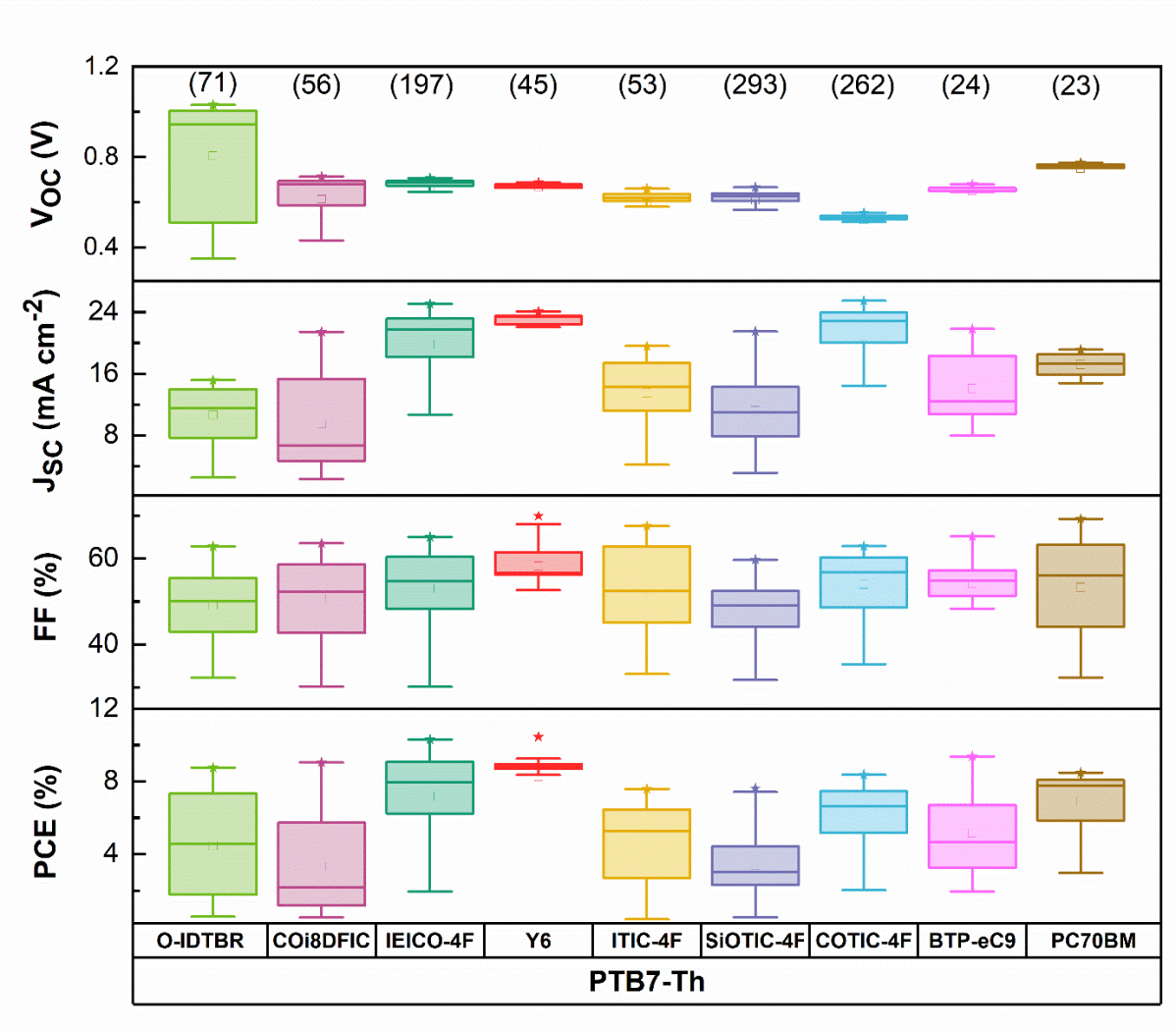

Figure 4. Box and whisker plot of photovoltaic parameters from more than 1000 devices of PTB7-Th blended with nine different acceptor materials. Data include variations in active layer thickness, annealing temperature, solvent additive, electron transport layer thickness, several casting temperatures, and various hole transport layer thicknesses. Statistical values are represented by mean (inner square), median (inner horizontal line), and maximum and minimum values (outer star and whisker height). The number of devices characterized for each material system is shown in brackets on the top row.

Charge recombination and collection in PTB7-Th based devices

Charge carrier recombination in the active layer of the OPVs is a known critical issue that affects free charge generation and transport. It can be assessed, at least in part, by studying the dependence of J_{SC} and V_{OC} on light intensity (P_{light}). The relationship between J_{SC} and P_{light} is well described by the formula of $J_{SC} \sim P_{light}^{\alpha}$, where the exponent α adopts different values depending on the degree of bimolecular recombination. The α exponent is close to 1 when there is no bimolecular recombination, whereas if bimolecular recombination becomes prominent,

then α is smaller than 1.[62] Figure 5a shows the fitted α values from log-log plots of J_{SC} *vs* P_{light} for all acceptor-PTB7-Th blends. For all cases α is close to unity, suggesting that there is almost no bimolecular recombination in PTB7-Th based devices. On the other hand, from the variation of V_{OC} with P_{light} one can infer the dominant recombination mechanism in OPVs. In the presence of strongly dominant bimolecular recombination, a slope of the curve V_{OC}-vs-log(P_{light}) equal to kT/q is expected. If bulk traps are present in the active layer, leading to trap-assisted recombination, an increase in that slope towards $2.kT/q$ is observed.[17] As shown in Figure 5b, the devices with low IE offset (≤0.5 eV) as for SiOTIC-4F, COTIC-4F, IEICO-4F, and COi8DFIC exhibit similar slopes of 1.20, 1.23, 1.26 and 1.28 kT/q, respectively, indicating moderate trap-assisted recombination. A higher trap recombination is observed for the devices with higher IE offset, that is O-IDTBR, Y6, BTP-eC9, $PC_{70}BM$, and ITIC-4F, which exhibit slope values of 1.34, 1.44, 1.49, 1.71, and 1.72 kT/q, respectively. Notably, this trend strongly correlates with their corresponding E_{loss} values (see Table 1).

To gain some insights into the charge extraction and collection processes, we also studied the dependence of the photocurrent density (J_{ph}) on the effective voltage (V_{eff}) of the devices. J_{ph} is calculated as the difference between light and dark *J-V* curves, $J_L - J_D$, whereas V_{eff} is calculated as $V_{eff} = V_0 - V_{bias}$, where V_0 is the voltage at which the photocurrent is equal to zero and V_{bias} is the applied bias. Figure 5c reveals that J_{ph} reaches the saturation value (J_{sat}) at around the same $V_{eff} \approx 2.0$ V for all systems. This indicates that all the photogenerated excitons have dissociated into free carriers and are collected by electrodes at high V_{eff}. From the ratio of J_{ph}/J_{sat} at short circuit conditions and at the maximum power point, the exciton dissociation efficiency (η_{diss}) and the charge collection efficiency (η_{coll}) Values of the *r* coefficient close to 1 indicate that both magnitudes are fully and linearly correlated, whereas values close to -1 means total anticorrelation. Figure 6 shows the Pearson correlation coefficient (*r*) matrix between each two pairs of relevant parameters in our study. Typically, the Spearman correlation coefficient (ρ) is often evaluated along with Pearson correlation to detect monotonic

but non-linear relationships of the ranked data within two features.[63] Figure S10 shows the plots of two variables against each other for $r > 0.5$. Figures S11-S13 show the correlation plots for V_{OC}, $J_{SC,}$ and FF, respectively, together with the calculated r and ρ values. In most cases, both Pearson and Spearman analysis show good agreement in identifying correlations between the considered parameters.

Generally speaking, the Pearson correlation matrix reveals that the IE offset has $|r| \geq 0.6$ with 7 out of 12 tested parameters, followed by E_g, recombination factor $n_{id,}$ and FF (6 out of 12), then E_{loss}, $E_{U,}$ and J_{SC} (5 out of 12).

Importantly, the IE offset is strongly correlated ($|r| \geq 0.88$) to E_g, E_{loss}, $E_{U,}$ and the trap-assisted recombination n_{id}, and to some extent to the dissociation ($r = 0.72$) and collection ($r = 0.58$) efficiencies (η_{diss} and η_{coll}). Note that, in general, E_{loss}, $E_{U,}$ and n_{id} are strongly correlated between themselves. As IE offset is a rather easy parameter to determine, before actually fabricating a solar cell, it is a very good predictor of performance in narrow gap OPVs.

The large correlation between IE offset and the electronic properties of the device (losses) makes this parameter a very good predictor of FF ($r = 0.80$). The device fill factor, a measure of the field dependence of charge generation, increases with the IE offset, suggesting that in low offset systems, charge generation exhibits a stronger dependence on the external bias. This observation is consistent with previous works.[38,39,49]

Besides the logical correlation between J_{SC} and bandgap, the photocurrent also depends on the IE and EA offsets. Moreover, decreasing IE offset can reduce the E_{loss}, minimize the $E_{U,}$ and suppress trap-assisted recombination n_{id}, thus improving the J_{SC} of devices, but it can also lead to insufficient driving force (lower values of η_{diss} and η_{coll}). This trade-off could be attributed to the interfacial energy level bending created by NFA molecular quadrupole moments, which act as an energy barrier for the acceptor exciton to charge-transfer state transition[49]

On the other hand, the band gap and the IE and EA offsets are highly correlated to V_{OC} as one may expect. Besides these energy levels, none of the other investigated parameters show a strong correlation to the open circuit voltage.

These findings reveal that energy offsets play a key role in charge photogeneration and recombination in low-bandgap OPVs. Importantly, they are good predictors for the three device parameters, V_{OC}, $J_{SC,}$ and FF, which may invite the use of simple density functional theory simulations and machine learning predictive models for the design of high-performance low-bandgap OPVs.

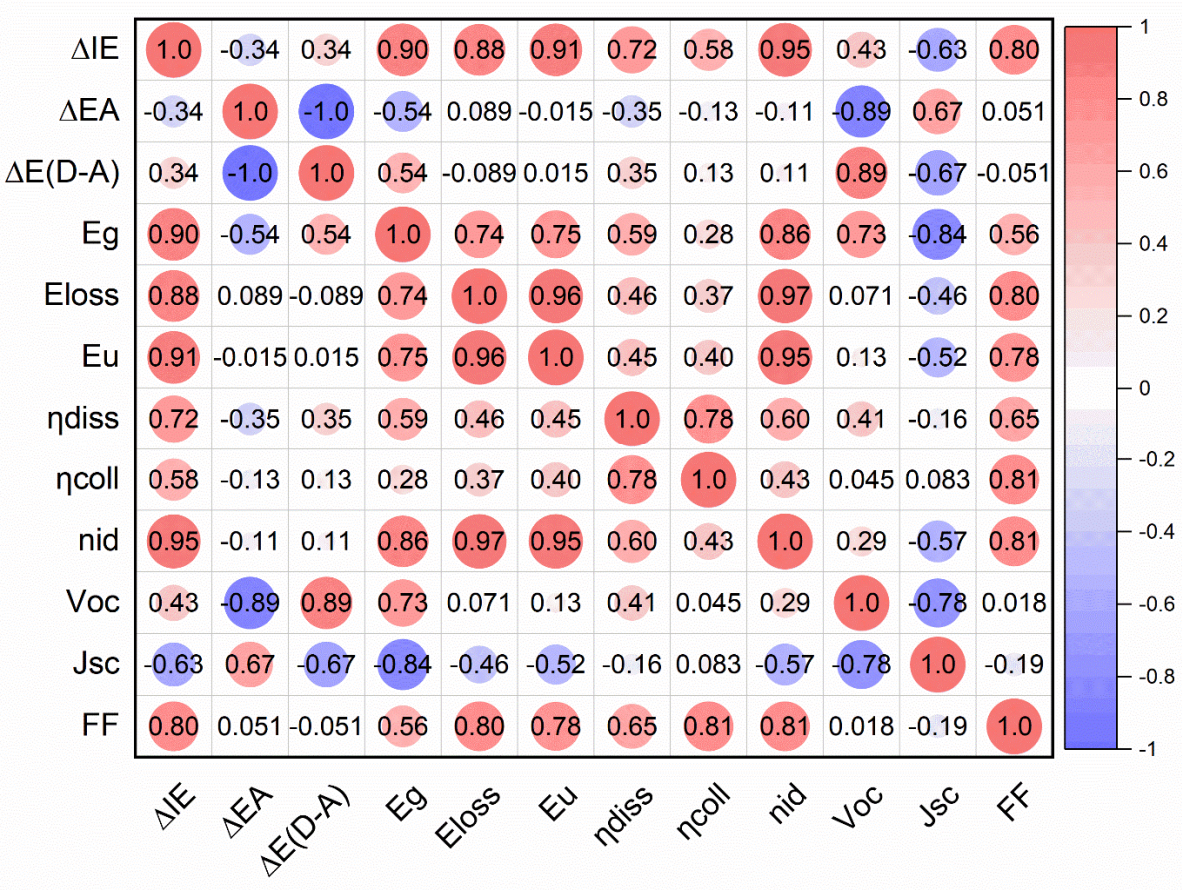

Figure 5. Multivariable Pearson correlation matrix between electronic features and photovoltaic figures-of-merit for PTB7-Th based blends.

CONCLUSION

In summary, we have demonstrated the synergic combination of high-throughput experimentation and statistical methods to effectively screen and understand the photovoltaic

potential of more than 2,000 doctor-bladed low-bandgap OPV devices. By screening 24 donor/acceptor low-bandgap material combinations including 5 different donors, we found that PTB7-Th based blends provide high efficiencies while DPP blends may be promising for solution-processed thick films in low-bandgap OPV devices, although exhibiting moderate PCE values. Despite NIP3T blends providing the lowest E_g values, more work has to be done to improve their performance, possibly in terms of energy level alignment, light harvesting capability and blend morphology. The analysis of variance allowed for ranking the sensitivity of the studied parameters to the performance of low-bandgap based devices. We found that materials selection and electronic features (*i.e.* electron affinity offset, ionization energy offset, band gap, and energy loss) had a more prominent impact on the final device performance than the processing conditions. These results were confirmed by more advanced correlation analysis based on Pearson and Spearman´s statistics. The detailed study of the effects of electronic descriptors from the most promising low-bandgap donor (*i.e.* PTB7-Th) demonstrated that there is a strong correlation between energy-level offsets and the resulting devices parameters, making the HOMO and LUMOs of the materials very effective and easily accessible predictors of device efficiency in narrow gap systems. Our study paves the way for the use of high-throughput experimentation and statistical methods to accelerate the material discovery of narrow-bandgap semiconductors in the energy field.

Conflict of interest

The authors declare there is no conflict of interest.

Acknowledgments

The authors acknowledge the financial support from the Spanish Ministerio de Ciencia e Innovación under Grants PID2021-128924OB-I00 in the framework of the Spanish R&D program Generacion de Conocimiento 2021, TED2021-131911B-I00 and CEX2019-000917-S

in the framework of the Spanish Severo Ochoa Centre of Excellence. X. R.-M. acknowledges the Alexander von Humboldt Foundation for funding his postdoctoral fellowship.

Received: ((will be filled in by the editorial staff))
Revised: ((will be filled in by the editorial staff))
Published online: ((will be filled in by the editorial staff))

References

[1] W. Liu, X. Xu, J. Yuan, M. Leclerc, Y. Zou, Y. Li, *ACS Energy Lett.* **2021**, *6*, 598.
[2] C. Yan, S. Barlow, Z. Wang, H. Yan, A. K.-Y. Jen, S. R. Marder, X. Zhan, *Nat Rev Mater* **2018**, *3*, 18003.
[3] G. Chai, Y. Chang, J. Zhang, X. Xu, L. Yu, X. Zou, X. Li, Y. Chen, S. Luo, B. Liu, F. Bai, Z. Luo, H. Yu, J. Liang, T. Liu, K. S. Wong, H. Zhou, Q. Peng, H. Yan, *Energy Environ. Sci.* **2021**, *14*, 3469.
[4] P. Cheng, G. Li, X. Zhan, Y. Yang, *Nature Photon* **2018**, *12*, 131.
[5] C. Guo, Y. Fu, D. Li, L. Wang, B. Zhou, C. Chen, J. Zhou, Y. Sun, Z. Gan, D. Liu, W. Li, T. Wang, *Advanced Materials* **2023**, *35*, 2304921.
[6] Z. Gan, L. Wang, J. Cai, C. Guo, C. Chen, D. Li, Y. Fu, B. Zhou, Y. Sun, C. Liu, J. Zhou, D. Liu, W. Li, T. Wang, *Nat Commun* **2023**, *14*, 6297.
[7] J. Wang, Z. Zheng, P. Bi, Z. Chen, Y. Wang, X. Liu, S. Zhang, X. Hao, M. Zhang, Y. Li, J. Hou, *National Science Review* **2023**, *10*, nwad085.
[8] H. Lu, W. Liu, G. Ran, Z. Liang, H. Li, N. Wei, H. Wu, Z. Ma, Y. Liu, W. Zhang, X. Xu, Z. Bo, *Angew Chem Int Ed* **2023**, e202314420.
[9] G. P. Kini, S. J. Jeon, D. K. Moon, *Adv Funct Materials* **2021**, *31*, 2007931.
[10] Y. Li, L. Zhong, B. Gautam, H.-J. Bin, J.-D. Lin, F.-P. Wu, Z. Zhang, Z.-Q. Jiang, Z.-G. Zhang, K. Gundogdu, Y. Li, L.-S. Liao, *Energy Environ. Sci.* **2017**, *10*, 1610.
[11] H. Cheng, Y. Zhao, Y. Yang, *Advanced Energy Materials* **2022**, *12*, 2102908.
[12] Z. Hu, J. Wang, X. Ma, J. Gao, C. Xu, K. Yang, Z. Wang, J. Zhang, F. Zhang, *Nano Energy* **2020**, *78*, 105376.
[13] Z. Jia, Q. Ma, Z. Chen, L. Meng, N. Jain, I. Angunawela, S. Qin, X. Kong, X. Li, Y. Yang, H. Zhu, H. Ade, F. Gao, Y. Li, *Nat Commun* **2023**, *14*, 1236.
[14] P. Cheng, H. Wang, R. Zheng, Y. Zhu, S. Dai, Z. Li, C. Chen, Y. Zhao, R. Wang, D. Meng, C. Zhu, K. Wei, X. Zhan, Y. Yang, *Advanced Materials* **2020**, *32*, 2002315.
[15] P. Cheng, Y. Liu, S.-Y. Chang, T. Li, P. Sun, R. Wang, H.-W. Cheng, T. Huang, L. Meng, S. Nuryyeva, C. Zhu, K.-H. Wei, B. Sun, X. Zhan, Y. Yang, *Joule* **2019**, *3*, 432.
[16] Y. Huang, L. Meng, H. Liang, M. Li, H. Chen, C. Jiang, K. Zhang, F. Huang, Z. Yao, C. Li, X. Wan, Y. Chen, *J. Mater. Chem. A* **2022**, *10*, 11238.
[17] A. A. A. Torimtubun, M. Méndez, E. Moustafa, J. Pallarès, E. Palomares, L. F. Marsal, *Solar RRL* **2023**, *7*, 2300228.
[18] Y. Li, Y. Cai, Y. Xie, J. Song, H. Wu, Z. Tang, J. Zhang, F. Huang, Y. Sun, *Energy Environ. Sci.* **2021**, *14*, 5009.
[19] S. Jung, Y. Cho, S.-H. Kang, S.-J. Yoon, C. Yang, *Solar RRL* **2022**, *6*, 2100819.
[20] Y. Xu, T. Zhang, H. Yao, J. Wang, P. Bi, J. Hou, *Journal of Energy Chemistry* **2022**, *72*, 388.
[21] Q. Li, Y. Guo, Y. Liu, *Chem. Mater.* **2019**, *31*, 6359.
[22] J. Huang, J. Lee, J. Vollbrecht, V. V. Brus, A. L. Dixon, D. X. Cao, Z. Zhu, Z. Du, H. Wang, K. Cho, G. C. Bazan, T. Nguyen, *Advanced Materials* **2020**, *32*, 1906027.

[23] F. Ullah, C.-C. Chen, W. C. H. Choy, *Adv Energy and Sustain Res* **2021**, *2*, 2000050.
[24] X. Rodríguez-Martínez, E. Pascual-San-José, M. Campoy-Quiles, *Energy Environ. Sci.* **2021**, *14*, 3301.
[25] L. Zhang, H. Zhao, B. Lin, J. Yuan, X. Xu, J. Wu, K. Zhou, X. Guo, M. Zhang, W. Ma, *J. Mater. Chem. A* **2019**, *7*, 22265.
[26] Y. Xiao, C. Zuo, J. Zhong, W. Wu, L. Shen, L. Ding, *Advanced Energy Materials* **2021**, *11*, 2100378.
[27] X. Zhang, H. Zhang, S. Li, L. Xiao, S. Zhang, B. Han, J. Kang, H. Zhou, *Nano Res.* **2023**, *16*, 11571.
[28] Z. Zheng, J. Wang, J. Ren, S. Wang, Y. Wang, W. Ma, L. Zheng, H. Li, Y. Tang, S. Zhang, J. Hou, *Sci. Adv.* **2023**, *9*, eadg9021.
[29] H. W. Ro, J. M. Downing, S. Engmann, A. A. Herzing, D. M. DeLongchamp, L. J. Richter, S. Mukherjee, H. Ade, M. Abdelsamie, L. K. Jagadamma, A. Amassian, Y. Liu, H. Yan, *Energy Environ. Sci.* **2016**, *9*, 2835.
[30] Y. Cho, B. Lee, S. Jung, S. Jeong, J. Park, G. Park, S. Yang, C. Yang, *Energy Environ. Sci.* **2023**, *16*, 6035.
[31] L. Zhang, B. Lin, B. Hu, X. Xu, W. Ma, *Advanced Materials* **2018**, *30*, 1800343.
[32] N. Yao, Q. Fan, Z. Genene, H. Liu, Y. Xia, G. Wen, Y. Yuan, E. Moons, J. Van Stam, W. Zhang, X. Lu, E. Wang, F. Zhang, *Solar RRL* **2023**, *7*, 2201134.
[33] A. Sánchez-Díaz, X. Rodríguez-Martínez, L. Córcoles-Guija, G. Mora-Martín, M. Campoy-Quiles, *Adv Elect Materials* **2018**, *4*, 1700477.
[34] E. Pascual-San-José, X. Rodríguez-Martínez, R. Adel-Abdelaleim, M. Stella, E. Martínez-Ferrero, M. Campoy-Quiles, *J. Mater. Chem. A* **2019**, *7*, 20369.
[35] X. Rodríguez-Martínez, E. Pascual-San-José, Z. Fei, M. Heeney, R. Guimerà, M. Campoy-Quiles, *Energy Environ. Sci.* **2021**, *14*, 986.
[36] A. Harillo-Baños, Q. Fan, S. Riera-Galindo, E. Wang, O. Inganäs, M. Campoy-Quiles, *ChemSusChem* **2022**, *15*, e202101888.
[37] M.-H. Lee, *Solar RRL* **2023**, *7*, 2300533.
[38] C. Yang, J. Zhang, N. Liang, H. Yao, Z. Wei, C. He, X. Yuan, J. Hou, *J. Mater. Chem. A* **2019**, *7*, 18889.
[39] J. Feng, G. Wen, R. Hu, J. Peng, H. Lu, N. Zhao, X. Zou, W. Zhang, *Solar RRL* **2023**, *7*, 2300372.
[40] G. Wen, R. Hu, J. Feng, J. Peng, Z. Chen, C. Zhang, N. Zhao, X. Zou, Z. Chen, C. Liu, W. Zhang, *Chemical Engineering Journal* **2023**, *475*, 145939.
[41] M. C. Scharber, N. S. Sariciftci, *Adv Materials Technologies* **2021**, *6*, 2000857.
[42] J. Bertrandie, J. Han, C. S. P. De Castro, E. Yengel, J. Gorenflot, T. Anthopoulos, F. Laquai, A. Sharma, D. Baran, *Advanced Materials* **2022**, *34*, 2202575.
[43] J. Lee, S. Ko, M. Seifrid, H. Lee, B. R. Luginbuhl, A. Karki, M. Ford, K. Rosenthal, K. Cho, T. Nguyen, G. C. Bazan, *Advanced Energy Materials* **2018**, *8*, 1801212.
[44] G. Zhang, Y. Fu, Z. Xie, Q. Zhang, *Solar Energy Materials and Solar Cells* **2011**, *95*, 1168.
[45] Y. Li, P. Sonar, S. P. Singh, M. S. Soh, M. Van Meurs, J. Tan, *J. Am. Chem. Soc.* **2011**, *133*, 2198.
[46] M. J. Alonso-Navarro, A. Harbuzaru, P. De Echegaray, I. Arrechea-Marcos, A. Harillo-Baños, A. De La Peña, M. M. Ramos, J. T. López Navarrete, M. Campoy-Quiles, R. Ponce Ortiz, J. L. Segura, *J. Mater. Chem. C* **2020**, *8*, 15277.
[47] Y. Patil, T. Jadhav, B. Dhokale, R. Misra, *Eur J Org Chem* **2016**, *2016*, 733.
[48] M. C. Scharber, D. Mühlbacher, M. Koppe, P. Denk, C. Waldauf, A. J. Heeger, C. J. Brabec, *Advanced Materials* **2006**, *18*, 789.
[49] S. Karuthedath, J. Gorenflot, Y. Firdaus, N. Chaturvedi, C. S. P. De Castro, G. T. Harrison, J. I. Khan, A. Markina, A. H. Balawi, T. A. D. Peña, W. Liu, R.-Z. Liang, A.

Sharma, S. H. K. Paleti, W. Zhang, Y. Lin, E. Alarousu, S. Lopatin, D. H. Anjum, P. M. Beaujuge, S. De Wolf, I. McCulloch, T. D. Anthopoulos, D. Baran, D. Andrienko, F. Laquai, *Nat. Mater.* **2021**, *20*, 378.
[50] M. I. Alonso, M. Campoy-Quiles, In *Ellipsometry of Functional Organic Surfaces and Films* (Eds.: Hinrichs, K.; Eichhorn, K.-J.), Springer International Publishing, Cham, **2018**, pp. 335–353.
[51] R. Ponce Ortiz, H. Herrera, M. J. Mancheño, C. Seoane, J. L. Segura, P. Mayorga Burrezo, J. Casado, J. T. López Navarrete, A. Facchetti, T. J. Marks, *Chemistry A European J* **2013**, *19*, 12458.
[52] K. S. Park, J. J. Kwok, R. Dilmurat, G. Qu, P. Kafle, X. Luo, S.-H. Jung, Y. Olivier, J.-K. Lee, J. Mei, D. Beljonne, Y. Diao, *Sci. Adv.* **2019**, *5*, eaaw7757.
[53] J. Yuan, D. Liu, H. Zhao, B. Lin, X. Zhou, H. B. Naveed, C. Zhao, K. Zhou, Z. Tang, F. Chen, W. Ma, *Advanced Energy Materials* **2021**, *11*, 2100098.
[54] X. Rodríguez-Martínez, C. Tormann, M. Sanz-Lleó, B. Dörling, M. Gibert-Roca, A. Harillo-Baños, A. A. A. Torimtubun, E. Pascual-San-José, J. P. Jurado, L. López-Mir, M. Kemerink, M. Campoy-Quiles, *to be published*.
[55] J. Vollbrecht, J. Lee, S.-J. Ko, V. V. Brus, A. Karki, W. Le, M. Seifrid, M. J. Ford, K. Cho, G. C. Bazan, T.-Q. Nguyen, *J. Mater. Chem. C* **2020**, *8*, 15175.
[56] N. Schopp, H. M. Luong, B. R. Luginbuhl, P. Panoy, D. Choi, V. Promarak, V. V. Brus, T.-Q. Nguyen, *ACS Energy Lett.* **2022**, *7*, 1626.
[57] N. Schopp, G. Akhtanova, P. Panoy, A. Arbuz, S. Chae, A. Yi, H. J. Kim, V. Promarak, T. Nguyen, V. V. Brus, *Advanced Materials* **2022**, *34*, 2203796.
[58] D. Zhang, B. Fan, L. Ying, N. Li, C. J. Brabec, F. Huang, Y. Cao, *SusMat* **2021**, *1*, 4.
[59] L. Zhan, S. Li, Y. Li, R. Sun, J. Min, Z. Bi, W. Ma, Z. Chen, G. Zhou, H. Zhu, M. Shi, L. Zuo, H. Chen, *Joule* **2022**, *6*, 662.
[60] S. F. Hoefler, G. Haberfehlner, T. Rath, A. Keilbach, M. A. Hobisch, A. Dixon, E. Pavlica, G. Bratina, G. Kothleitner, F. Hofer, G. Trimmel, *ACS Appl. Energy Mater.* **2019**, *2*, 7535.
[61] X. Xu, Q. Wei, Z. Zhou, H. He, J. Tian, H. Yip, Y. Fu, X. Lu, Y. Zhou, Y. Li, Y. Zou, *Adv Funct Materials* **2023**, 2305017.
[62] A. A. A. Torimtubun, J. G. Sánchez, J. Pallarès, L. F. Marsal, *Sustainable Energy Fuels* **2020**, *4*, 3378.
[63] P. Schober, C. Boer, L. A. Schwarte, *Anesthesia & Analgesia* **2018**, *126*, 1763.

High-throughput experimentation and statistical methods are leveraged to evaluate the photovoltaic potential of 24 low-bandgap blends. The extensive dataset (more than 2,000 devices) is subjected to parameter sensitivity and correlation studies to find out the most influential features. The strong correlation between the energy offsets and photovoltaic parameters makes the former excellent efficiency predictors for low-bandgap solar cells.

Alfonsina Abat Amelenan Torimtubun,[a] Matías-Jesús Alonso Navarro,[b,c] Arianna Quesada-Ramírez,[a] Xabier Rodríguez-Martínez,[d] José L. Segura,[b] Alejandro R. Goñi*[a,e] and Mariano Campoy-Quiles*[a]

High-Throughput Screening of Low-Bandgap Organic Semiconductors for Photovoltaic Applications: In the Search for Correlations

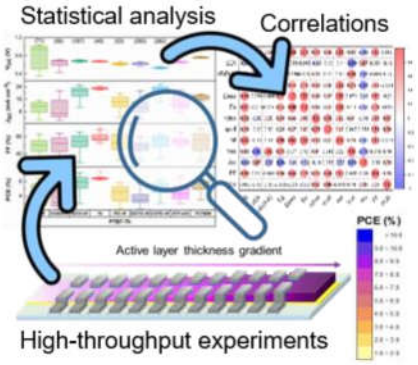

EQE data for completeness

Click here to access/download

Data File

EQE.rar

Figures for completeness

Click here to access/download

Data File

Figures.rar

JV curves for completeness

Click here to access/download

Data File

J-V.rar

Table of contents figure suggestion